ADVANCED MATERIALS INTERFACES
www.advmatinterfaces.de

Terahertz Spin-to-Charge Current Conversion in Stacks of Ferromagnets and the Transition-Metal Dichalcogenide $NbSe_2$

Lukáš Nádvorník, Oliver Gueckstock, Lukas Braun, Chengwang Niu, Joachim Gräfe, Gunther Richter, Gisela Schütz, Hidenori Takagi, Mahmoud Zeer, Tom S. Seifert, Peter Kubaščík, Avanindra K. Pandeya, Abdelmadjid Anane, Heejun Yang, Amilcar Bedoya-Pinto, Stuart S. P. Parkin, Martin Wolf, Yuriy Mokrousov, Hiroyuki Nakamura, and Tobias Kampfrath*

Transition-metal dichalcogenides (TMDCs) are an aspiring class of materials with unique electronic and optical properties and potential applications in spin-based electronics. Here, terahertz emission spectroscopy is used to study spin-to-charge current conversion (S2C) in the TMDC $NbSe_2$ in ultra-high-vacuum-grown F|$NbSe_2$ thin-film stacks, where F is a layer of ferromagnetic Fe or Ni. Ultrafast laser excitation triggers an ultrafast spin current that is converted into an in-plane charge current and, thus, a measurable THz electromagnetic pulse. The THz signal amplitude as a function of the $NbSe_2$ thickness shows that the measured signals are fully consistent with an ultrafast optically driven injection of an in-plane-polarized spin current into $NbSe_2$. Modeling of the spin-current dynamics reveals that a sizable fraction of the total S2C originates from the bulk of $NbSe_2$ with the opposite, negative sign of the spin Hall angle as compared to Pt. By a quantitative comparison of the emitted THz radiation from F|$NbSe_2$ to F|Pt reference samples and the results of ab initio calculations, it is estimated that the spin Hall angle of $NbSe_2$ for an in-plane polarized spin current lies between –0.2% and –1.1%, while the THz spin-current relaxation length is of the order of a few nanometers.

1. Introduction

Transition-metal dichalcogenides[1] (TMDCs) are an emerging class of materials with a C-TM-C stacking structure, where C and TM, respectively, denote a chalcogen atom (such as Se or S) and a transition-metal atom (such as Nb, W, or Mo). In the last decade, TMDC monolayers have attracted considerable attention[2–12] owing to their unique combination of electronic and optical properties. The hexagonal crystal structure of such quasi-two-dimensional materials implies inequivalent K-valleys in their electronic band structure, which gives rise to the valley degree of freedom and valley-based electronic functionalities (valleytronics).[13] The TM atoms provide large spin-orbit coupling (SOC),[14] which leads to further unique properties such as spin-valley locking,[15] selective excitation of

L. Nádvorník, O. Gueckstock, T. S. Seifert, T. Kampfrath
Department of Physics
Freie Universität Berlin
14195 Berlin, Germany
E-mail: nadvornik@karlov.mff.cuni.cz

L. Nádvorník, P. Kubaščík
Faculty of Mathematics and Physics
Charles University
Prague 121 16, Czech Republic

O. Gueckstock, L. Braun, M. Wolf, T. Kampfrath
Department of Physical Chemistry
Fritz Haber Institute of the Max Planck Society
14195 Berlin, Germany

The ORCID identification number(s) for the author(s) of this article can be found under https://doi.org/10.1002/admi.202201675.

DOI: 10.1002/admi.202201675

C. Niu, M. Zeer, Y. Mokrousov
Peter Grünberg Institut
Forschungszentrum Juelich
D-52425 Juelich, Germany

C. Niu
School of Physics
State Key Laboratory of Crystal Materials
Shandong University
Jinan 250100, China

J. Gräfe, G. Richter, G. Schütz, H. Takagi, H. Nakamura
Department of Quantum Materials
Max Planck Institute for Solid State Research
70569 Stuttgart, Germany

M. Zeer
Department of Physics
RWTH Aachen University
52056 Aachen, Germany

A. K. Pandeya, A. Bedoya-Pinto, S. S. P. Parkin
NISE Department
Max Planck Institute for Microstructure Physics
Saale, 06120 Halle, Germany

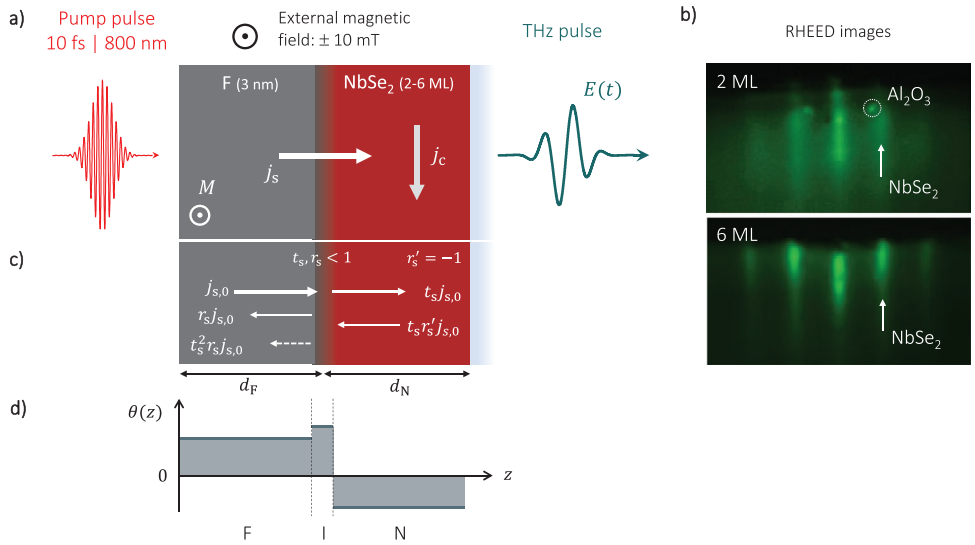

Figure 1. Schematic of laser-induced THz emission from F|$NbSe_2$ stacks. a) A F|$NbSe_2$ thin-film stack consisting of a metallic ferromagnetic layer F = Fe or Ni with magnetization *M* on top of a layer of the metallic TMDC $NbSe_2$ (thickness of 2–6 ML) is excited by a femtosecond laser pulse. The resulting spin voltage injects an ultrashort spin-polarized spin current j_s from F into the adjacent $NbSe_2$. Spin-orbit coupling converts j_s into a perpendicular charge current j_c. The resulting THz electric field $E(t)$ is detected by electro-optic sampling yielding a THz signal $S(t)$. b) RHEED images of 2 ML and 6 ML of $NbSe_2$, taken in situ during the hybrid-PLD growth. c) Schematic of the spin-current echoes flowing through the F|N interface with interface transmission and reflection coefficients $t_s, r_s < 1$ and $r_s' = -1$ at the interface to the substrate. d) Illustration of regions with notable S2C, each characterized by its own spin Hall angle $\theta(z)$.

the valley and spin polarizations,[16] large spin-orbit torque,[17] and a large valley Hall effect.[18] The combination of valley-dependent physics and pronounced SOC makes TMDCs excellent candidates for spintronic, opto-spintronic, and valleytronic applications.

Most spin-related features of TMDCs, in particular optical spin injection[16], are uniquely associated with the out-of-plane spin orientation. In contrast, in-plane spin dynamics have received attention only in recent works,[17,19,20] in which spin pumping was used to measure spin-orbit torque or the interface-related Rashba–Edelstein effect in ferromagnet|TMDC bilayers. On the other hand, only a few studies directly addressed the spin Hall effect,[21] the conversion of a longitudinal charge current into a perpendicular spin current, or its inverse.[22] The in-plane spin geometry is particularly favorable for the observation of the SHE in TMDCs as the valley Hall effect is not operative in this geometry.

Terahertz (THz) emission spectroscopy is an excellent tool to study such spin transport phenomena and spin-to-charge current conversion (S2C) on their natural, i.e., ultrafast, time scales in, for example, fully metallic[23–28] or insulating-magnet|normal-metal heterostructures[29–31] and newly emerging materials like TMDCs.[22,32] An interesting application is the versatile optical generation of broadband THz electromagnetic pulses.[24,33,34] As shown in **Figure 1**a, the operation of such metallic spintronic THz emitters is based on the optically triggered generation of a spin voltage (spin accumulation) in the magnetic layer.[35,36] It drives a spin current that is transformed into a transverse charge current by ultrafast S2C, resulting in the emission of an electromagnetic pulse with frequencies extending into the THz range.[24,36–38] The THz emission approach is also useful to approximately determine the relative strength of ultrafast S2C of materials in a contact-free and rapid manner.[24,39–41]

In this work, we address ultrafast spin transport and S2C in F|TMDC stacks, where F is a metallic ferromagnetic layer F of Fe or Ni, and the TMDC layer is $NbSe_2$. Following optical excitation of F|$NbSe_2$, we observe emission of THz pulses with sizable amplitude. The temporal dynamics and $NbSe_2$-thickness dependence of the emitted THz electric field are fully consistent with the notion that optical excitation drives an ultrafast in-plane-polarized spin current into the bulk of $NbSe_2$. A qualitative comparison to a spin-transport model indicates that the TMDC, the ferromagnet, and, possibly, their interface contribute significantly to the total S2C. A comparison to F|Pt reference samples allows us to make a quantitative estimate

A. Anane
Unité Mixte de Physique
CNRS
Thales
Univ. Paris-Sud
Université Paris-Saclay
Palaiseau 91767, France
H. Yang
Department of Physics
Korea Advanced Institute of Science and Technology (KAIST)
Daejeon 34141, Korea
A. Bedoya-Pinto
Institute of Molecular Science (ICMol)
University of Valencia
Paterna 46980, Spain
Y. Mokrousov
Institute of Physics
Johannes Gutenberg University Mainz
55099 Mainz, Germany
H. Nakamura
Physics Department
University of Arkansas
Fayetteville, AR 72701, USA

of the spin Hall angle and spin current relaxation length of $NbSe_2$ at THz frequencies, yielding –(0.2–1.1)% and 0.9–6 nm, respectively. Ab initio calculations are fully consistent with the obtained range of spin Hall angles.

2. Results and Discussion

2.1. Samples

The basic structure F|N of our samples is shown in Figure 1a, where F and N are ferromagnetic and normal-metal layers, respectively. For clarity, all samples are always shown in this form even though the substrate is on the right-hand side. Atomically thin films of N=$NbSe_2$ are grown in the 2H phase by hybrid pulsed-laser deposition (hybrid-PLD)[42,43] on double-side-polished sapphire substrates. Images of reflective high-energy electron diffraction (RHEED) taken after the $NbSe_2$ growth (Figure 1b) indicate 2D layer-by-layer growth. The TMDC layer is covered by a layer of a ferromagnetic metal F (thickness of 3 nm) and finally capped by an AlO_x protection layer (2 nm). Details on the sample preparation can be found in the Experimental Section.

Note that S2C can, in principle, take place in any plane located at a depth z of the F|$NbSe_2$ stack (Figure 1d). To extract the charge-current amplitude inside the $NbSe_2$ layer, we study samples with F = Fe or Ni, which feature opposite spin Hall angles ($\theta_{Fe} < 0$ and $\theta_{Ni} > 0$),[44] and $NbSe_2$ thicknesses d_N between 2 and 6 monolayers (MLs), where 1 ML = 0.65 nm. For quantitative analysis, the sample set is complemented by two reference samples F|Pt, in which $NbSe_2$ is replaced by Pt (3 nm) providing a large $\theta_{Pt} \approx 10\%$.[21,45] The in-plane magnetization of all F layers is controlled by an external magnetic field with a strength of about ±10 mT.

2.2. Methodology

Our methodology is based on the detection of spin currents j_s and S2C by measuring the emitted THz electric field $E(t)$ (Figure 1a). The F|N samples with F = Ni or Fe and N = $NbSe_2$ or Pt are excited by near-infrared femtosecond laser pulses (duration of 10 fs, center wavelength of 800 nm, pulse energy of ≈1 nJ, repetition rate of 80 MHz) from the substrate side. For clarity and without loss of validity, the schematic (Figure 1a) shows the pump pulse on the opposite side (see above).

As observed previously,[24–26,36,38,40,45–53] excitation of F|N stacks leads to an out-of-plane spin current j_s with polarization parallel to the F magnetization M, which is converted into an in-plane charge current j_c by S2C, thereby, generating an electromagnetic pulse with transient electric field $E(t)$ directly behind the sample. Note that, here, j_s and j_c have the same dimension of $m^{-2}\ s^{-1}$. To probe $E(t)$, the emitted THz pulse is focused on a ZnTe(110) crystal (thickness of 1 mm) and detected by electro-optic sampling.[54,55] All experiments are performed at room temperature under ambient conditions.

In the frequency domain and in the thin-film approximation,[24,56,57] the complex-valued THz field amplitude due to ultrafast spin transport and S2C is given by

$$E(\omega) = eZ(\omega)\int \mathrm{d}z\ j_c(z,\omega) = eZ(\omega)\int \mathrm{d}z\ \theta(z)\, j_s(z,\omega) \quad (1)$$

Here, z is the coordinate along the sample normal (Figure 1a), $\omega/2\pi$ is frequency, Z is the total sample impedance, and $\theta(z)$ is the local spin Hall angle that characterizes the strength of S2C. In Equation (1), the total integrated charge sheet current $I_c = \int \mathrm{d}z\ j_c(z)$ has, in principle, contributions from all layers and their interfaces, depending on the local value of $j_s(z)$ and $\theta(z)$. Guided by Figure 1d and ref. [40], we assume that $\theta(z)$ can be characterized by three S2C values: θ_F for the F bulk, θ_N for the N bulk, and θ_I for the F/N interface I. It follows that I_c equals the sum

$$I_c = \theta_N J_N + \theta_I J_I + \theta_F J_F \quad (2)$$

where $J_i = \int_i \mathrm{d}z\ j_s(z)$ is the sheet spin current integrated over the respective layer i = N, I or F. We note that, in this geometry, similar to spin-pumping experiments at GHz frequencies,[30] the valley Hall effect is not operative due to the in-plane spin polarization of j_s.[18]

2.3. Raw THz Emission Signals

Figure 2 shows raw THz waveforms emitted from F|$NbSe_2$ bilayers with varying thickness and for F = Fe or Ni, complemented by comparison to their respective reference samples F|Pt. A typical THz waveform obtained from Fe|$NbSe_2$(6 ML) is displayed in Figure 2a. Here, the THz signal $S(t, M)$ almost fully reverses upon reversal of the magnetization M of the Fe layer (solid and dashed waveforms), indicating the magnetic origin of the THz emission. As we are interested in effects odd in M, we focus on the signal $S_-(t) = [S(t, +M) - S(t, -M)]/2$ in the following. We also observe an even component $S_+(t) = [S(t, +M) + S(t, -M)]/2$, which is typically an order of magnitude smaller than the odd component (see Figure S1, Supporting Information). It can originate from all photocurrents relying on broken inversion symmetry at interfaces or surfaces, for example, injection- or shift-current mechanisms.[36]

The THz amplitude scales linearly with the energy of the optical pump (Figure S2, Supporting Information). This behavior is typical for a photocurrent in the small-perturbation regime. Reversal of the sample (pump from metallic side as depicted in Figure 1a) leads to reversal of the THz signal (see Figure S3, Supporting Information), consistent with a spin current flowing from F to N.[40] We do not observe detectable changes in the THz emission for linearly polarized pump pulses compared to left or right-handed circular polarizations. All these observations confirm the emission scenario summarized in Figure 1a.

Figure 2b,c shows the signals $S_-(t)$ from Fe|$NbSe_2$ and Ni|$NbSe_2$ for d_N = 2, 3, 4, 6 ML and their respective F|Pt references. We make four observations: (i) The THz signals from F|$NbSe_2$ are reversed when F = Fe is replaced by Ni. In contrast, the signals from the reference F|Pt do not reverse. (ii) The amplitude of the emitted waveforms depends on d_N. The trend of the absolute value of the amplitude is, however, opposite for sample sets with F = Fe (Figure 2b) and Ni (Figure 2c),

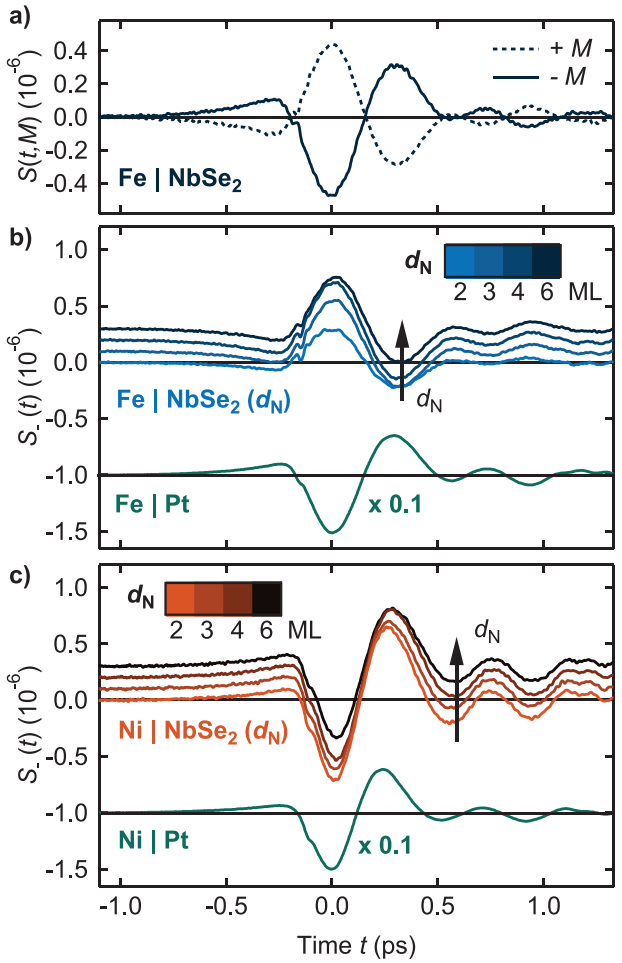

Figure 2. THz emission from F|$NbSe_2$ stacks and F|Pt reference samples. a) THz electro-optic signals $S(t, \pm M)$ from Fe|$NbSe_2$(6 ML) for opposite orientation of the in-plane Fe magnetization M. b) Antisymmetric component $S_-(t)$ with respect to M for Fe|$NbSe_2$(d_N) (upper blue curves) with d_N = 2, 3, 4, and 6 ML, where the arrow indicates the increasing d_N. The signal from the reference sample Fe|Pt (lower green curve) is also shown and vertically offset and scaled by 0.1 for clarity. c) Same as panel b) but for F = Ni (orange curves). Curves in (b,c) are vertically offset for clarity.

where, respectively, $|S_-|$ increases and decreases with d_N. (iii) The THz signal amplitudes of F|$NbSe_2$ are generally one order of magnitude smaller than those from their F|Pt references. (iv) Apart from this scaling factor, the temporal shape of all traces (Figure 2b,c) is very similar.

Observation (iv) indicates that the driving force of the THz spin current in F|$NbSe_2$ and F|Pt is the same, that is, a transient spin voltage.[35] Consequently, we can omit the time-dependence of the THz signal and use the root-mean square (RMS) of $S_-(t)$ as an adequate measure of the emission strength. Feature (i) suggests that the signal reversal is related to the only varying layer, that is, layer F, due, for example, to the opposite sign of θ_{Fe} and θ_{Ni}. Together with feature (iii) and by using Equation (2), we can conclude without any quantitative analysis that S2C in our F|$NbSe_2$ samples is not, unlike in F|Pt, dominated by the non-ferromagnetic layer and, thus, significantly affected by S2C inside F or at the interface. However, observation (ii) suggests a sizable contribution to S2C from the TMDC as well.

2.4. Normalized Signals versus $NbSe_2$ Thickness

To address the impact of the TMDC thickness, we normalize the RMS of the traces $S_-(t)$ in Figure 2b,c by the independently measured impedance Z and pump absorbance A[30,40] for each sample (see Figure S4, Supporting Information). Owing to Equation (1), the resulting quantity rms I_c is the RMS of the THz sheet charge current $I_c(t) = \int dz\, j_c(z,t)$ (see Figure 1) normalized by the absorbed pump energy.

Figure 3 shows rms I_c for the Fe and Ni sample sets. We observe that rms I_c in Ni|$NbSe_2$ is generally larger than in Fe|$NbSe_2$, for example, by a factor of ≈ 1.5 for d_N = 3 nm. Figure 3 also reveals a non-trivial trend of rms I_c as a function of d_N. While rms I_c versus d_N is non-monotonic in the case of Fe|$NbSe_2$ (Figure 3a), it monotonically decreases for Ni|$NbSe_2$ (Figure 3b). Considering that the charge current I_c can originate from both layers and their interface (see Equation (2)), this observation allows us to draw an immediate conclusion. If I_c was fully generated by the S2C solely inside the F bulk or at the F/N interface, the A-normalized rms I_c would decrease monotonically with increasing d_N because a smaller fraction of pump-pulse energy would be deposited in F and, thus, a smaller j_s would be triggered. While such a monotonic decrease is observed for Ni|$NbSe_2$ (Figure 3b), it is not for Fe|$NbSe_2$

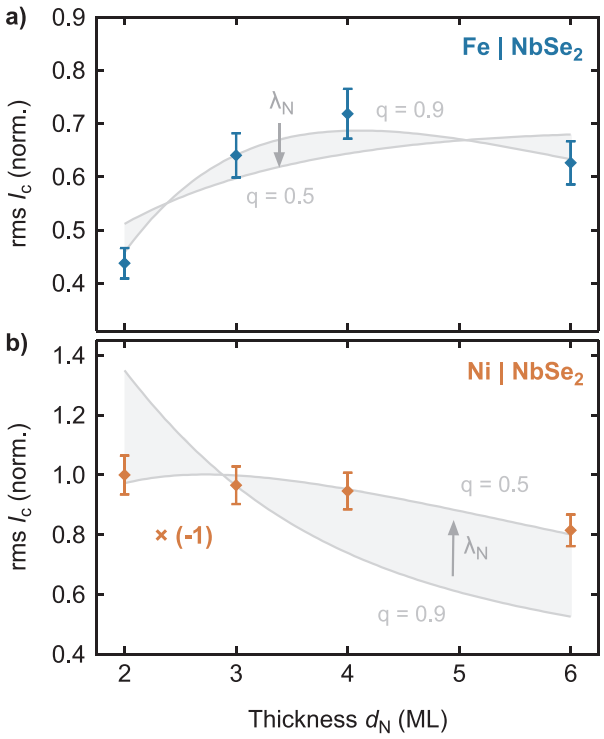

Figure 3. Impact of the TMDC layer on total S2C. a) RMS amplitudes, rms I_c, of the sheet charge current I_c, normalized to the absorbed pump-pulse energy, versus $NbSe_2$ thickness d_N for Fe|$NbSe_2$ and b) Ni|$NbSe_2$ stacks. For clarity, the amplitudes in panel b) are multiplied by –1 and rescaled by a global factor to achieve $I_c(d_N = 2\ ML) = 1$. The gray areas represent fits according to the transport model for varying spin-current relaxation lengths λ_N = 0.9–5.8 nm (indicated by gray arrows) and weighting factor q = 0.9. The curve corresponding to the largest λ_N also overlaps with the solution for q = 0.5 and λ_N = 5.8 nm (see Table S1, Supporting Information).

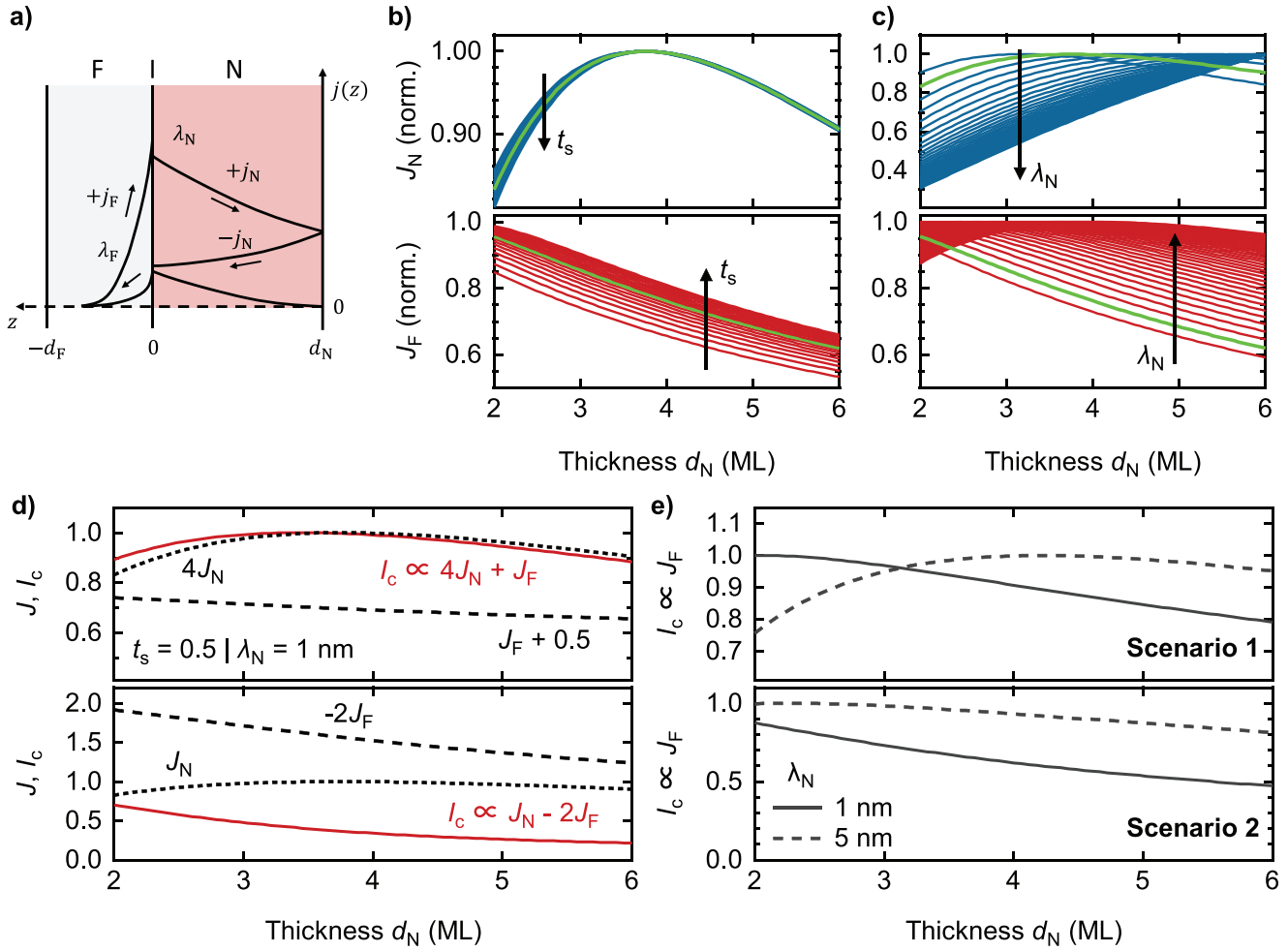

Figure 4. Model of spin-current propagation and qualitative analysis. a) Schematic of the z-dependence of the spin-current densities $j_N(z)$ and $j_F(z)$, capturing the exponential decay of $j_N(z)$ on the relaxation length λ_N, and multiple reflections from a semitransparent F/N interface with spin transmission coefficient t_s. b) Layer-integrated spin currents in the non-magnetic layer (J_N, top panel) and ferromagnet (J_F, bottom panel) as a function of the $NbSe_2$ thickness d_N for $\lambda_N = 1$ nm and varying $t_s = 0.1$–0.9 (increase depicted by arrows). c) J_N and J_F for $t_s = 0.5$ and varying $\lambda_N = 0.8$–8 nm. Curves calculated for default values $t_s = 0.5$, $\lambda_N = 1$ nm and the ratio $B = 1$ of relative absorptivity are plotted in green in panels (b) and (c). d) Two examples of linear combinations of J_N and J_F, both calculated for default values $t_s = 0.5$ and $\lambda_N = 1$ nm, leading to different dependencies of the total charge current I_c versus d_N. e) Construction of a non-monotonic trend of I_c (scenario 1) and a monotonically decreasing trend (scenario 2) by assuming that the transport is totally dominated by the current in F ($I_c \propto J_F$). Calculations are done for $\lambda_N = 1$ nm, where a non-monotonic trend cannot be achieved within the parameter range of $t_s = 0.1$–0.9 and $B = 0.5$–2 (scenario 1: $t_s = 0.9$, $B = 0.5$; scenario 2: $t_s = 0.5$, $B = 2$). For $\lambda_N = 5$ nm, a monotonic trend is possible (scenario 1: $t_s = 0.8$, $B = 1$; scenario 2: $t_s = 0.4$, $B = 1$).

(Figure 3a). Therefore, at least for Fe|$NbSe_2$, I_c is not exclusively generated in the ferromagnet or at the F/N interface. In other words, the I_c contribution from S2C inside N is non-zero, and the spin current j_s must be injected into the bulk of $NbSe_2$.

The monotonic and non-monotonic trends of I_c versus d_N for the Ni and Fe sample sets suggest that the sheet spin currents J_i in the three regions $i = F, N, I$ have a different d_N-dependence. If the corresponding S2C strengths θ_i in these regions differ, the linear combination $\sum J_i \theta_i$ (Equation (2)) can yield a non-trivial and distinct I_c versus d_N. The distinctly different d_N-dependence of I_c for the Ni and Fe sample sets is addressed in detail in the following sections: A spin-transport model is introduced in Section 2.5, followed by a qualitative argumentation in Section 2.6 and a quantitative analysis by fitting in Section 2.7.

2.5. Spin-Current Model

To gain further insight into each individual S2C contribution, we model $j_s(z)$, express the resulting I_c using Equation (2) and compare it to the data shown in Figure 3. For this purpose, we assume that the pump pulse drives a spin current j_s that is initially incident on the F/N interface with an amplitude j_{s0} (see Figures 1c and 4a). Subsequently, j_s is partially reflected at the semitransparent F/N interface (spin transmission coefficient $0 < t_s < 1$, reflection coefficient $r_s = t_s - 1$, thus $-1 < r_s < 0$) and decays exponentially with the relaxation length λ_i. For the $NbSe_2$/substrate interface, we assume total reflection with $r_s' = -1$. From previous works,[24,58] we infer $\lambda_F \sim 1$ nm, which is smaller than the F-layer thickness $d_F = 3$ nm. Therefore, we can neglect reflections off the left F boundary (Figure 4a).

By summing up all reflection echoes, we obtain the integrated spin currents $J_N = \int_N dz\, j_s(z)$ and $J_F = \int_F dz\, j_s(z)$ (see Experimental Section) in the form

$$J_N(d_N) = j_{s0}\lambda_N \frac{\left(e^{d_N/\lambda_N}-1\right)^2}{e^{2d_N/\lambda_N}-r_s}$$
$$J_F(d_N) = j_{s0}\lambda_F\left[1-t_s\frac{1}{e^{2d_N/\lambda_N}-r_s}\right] \quad (3)$$

where j_{s0} is the total spin current incident on the F/$NbSe_2$ interface and directly proportional to the pump-induced spin voltage of F. Because the spin voltage, in turn, is proportional to the density of the absorbed pump power in F, we use the scaling $j_{s0} \propto A/(d_F + Bd_N)$, where $B = \mathrm{Im}(n_N^2)/\mathrm{Im}(n_F^2)$ stands for the relative absorptivity of the N and F material.[35] According to previous work,[59–61] the B of our samples is approximately 1 with, however, substantial variation with $NbSe_2$ thickness and quality. We now make use of Equation (2) to investigate the relative importance of the parameters t_s, λ_N, B and θ_i for the d_N-dependence of the normalized charge sheet current density I_c (Figure 3). This approach will eventually provide us with upper and lower limits to the spin Hall angle and λ_N of $NbSe_2$.

Figure 4b,c show calculated values of J_N and J_F vs the experimental range of d_N for $B = 1$ and various t_s = 0.1–0.9 and λ_N = 0.8–8 nm, respectively. We see that, for all considered t_s, J_N is non-monotonic, whereas J_F keeps its monotonic behavior (Figure 4b). Our calculations indicate a qualitatively similar and, thus, a small impact on the variation of B. Similarly, spin memory loss at the interface (captured by $a = t_s - 1 - r_s \neq 0$) is a minor effect, too (see Figure S5, Supporting Information). In contrast, variation of λ_N has a stronger impact on J_N and J_F. For $\lambda_N > 2$ nm, $J_N(d_N)$ changes to a monotonically increasing trend, and a non-monotonic dependence of $J_F(d_N)$ appears for $\lambda_N > 4$ nm in the relevant d_N interval.

Finally, according to Equation (2), the total sheet charge current I_c is determined by a linear combination of the sheet spin current densities $J_N(d_N)$ and $J_F(d_N)$, where θ_N and θ_F play the role of weight factors,

$$I_c = J_F(d_N)\theta_F(1+\nu_{F/N}) + J_N(d_N)\theta_N \quad (4)$$

Here, the first term proportional to J_F captures the S2C in both the F bulk and at the F/$NbSe_2$ interface, where $\nu_{F/N} = d_I/\lambda_F$ denotes the relative contribution of the interface with effective thickness d_I. To stress this fact, we can define an effective spin Hall angle $\theta_F' = \theta_F(1+\nu_{F/N})$ that includes the bulk and interfacial S2C. An illustration of qualitatively different results with non-monotonic and monotonically decreasing trends versus d_N for different linear combinations $I_c = 4J_N + J_F$ and $I_c = J_N - 2J_F$ and default values $t_s = 0.5$ and $B = 1$ is shown by the black solid curves in Figure 4d. This graph is the basis for further qualitative interpretation of our measurements.

2.6. Qualitative Comparison

We first limit our discussion to cases with $\lambda_N \leq 4$ nm. Such an assumption is realistic because larger THz spin-current relaxation lengths in spintronic THz emission were not observed so far, including materials with negligible spin-orbit interaction like Cu.[24,28,40,45,58] In this case, J_F shows only a monotonically decreasing trend with d_N (Figure 4b,c) and cannot explain the measured non-monotonic d_N-dependence of Fe|$NbSe_2$ (Figure 3a). Thus, I_c requires a relatively strong contribution from J_N, implying that the spin Hall angle θ_N is comparable or larger than θ_F'. In other words, there is a sizable component of S2C in the bulk of $NbSe_2$.

To confirm the robustness of this qualitative conclusion, we assume that both Fe- and Ni-based sample sets may have different model parameters t_s and B. By varying these parameters within realistic intervals 0.1–0.9 and 0.5–2, respectively, we aim to obtain a non-monotonic trend of I_c versus d_N, as observed in Fe-based samples, without the contribution of J_N (taking $\theta_N = 0$). As documented by the solid lines in Figure 4e (scenarios 1 and 2), the results cannot capture the required dependence without considering a sizable θ_N, even for the extreme values of t_s and B.

The situation may change if we assume $\lambda_N > 4$ nm. In this case, J_F versus d_N can reach a non-monotonic trend. By choosing sufficiently different model parameters for scenario 1 ($t_s = 0.8$, $B = 1$) and scenario 2 ($t_s = 0.4$, $B = 1$), we can model qualitatively the same d_N-dependence of I_c without any contribution of J_N. A similar discussion with respect to variations of the spin-memory-loss parameter leads to a qualitatively identical conclusion as for the variation of t_s (see Figure S5, Supporting Information).

To summarize, our modeling can reproduce the measured d_N-dependence of the normalized rms I_c (Figure 3) for only two scenarios: In scenario 1, the spin current is converted in the bulk of the TMDC with sizable θ_N and has a relaxation length $\lambda_N < 4$ nm. In scenario 2, there is no significant S2C in the TMDC, the spin current has $\lambda_N > 4$ nm, and the spin transmission coefficients of the Fe/$NbSe_2$ and Ni/$NbSe_2$ interfaces differ by a factor of 2.

2.7. Fitting of $I_c(d_N)$

After identifying two theoretically possible scenarios of spin current propagation, we can now roughly estimate the absolute magnitude of θ_N and λ_N by simultaneously fitting Equation (4) to both data sets of the A-normalized rms I_c versus d_N in Figure 3a,b. The fit minimizes the weighted sum of the squares R^2 of both data sets $qR^2_{Fe|NbSe_2} + (1-q)R^2_{Ni|NbSe_2}$ with the relative weight q that allows us to prioritize one of the trends. Because the normalized data are determined up to a global scaling factor, the fitting process yields only the relative proportion $\theta_{NbSe_2} : \theta_{Fe}' : \theta_{Fe}$. To obtain the absolute value of the spin Hall angles, we compare it to the A-normalized rms I_c of the reference samples Fe|Pt and Ni|Pt (Figure 2b,c) and use $\theta_{Pt} \approx 10\%$[21], as detailed in the Experimental Section.

To minimize the number of fitting parameters and simplify the model, we fix the default values of $t_s = 0.5$, $B = 1$, $a = 0$ for both the Fe- and Ni-based sample sets. We first evaluate the fits for selected values of λ_N = 0.9–5.8 nm. They are shown in Figure 3 by the light-gray-shaded area, whose boundaries represent the extremal λ_N. To better capture the characteristic

Table 1. Results of the fitting procedure of the *A*-normalized rms I_c versus d_N in Figure 3a,b. The extracted spin Hall angles are θ_{NbSe_2} for bulk $NbSe_2$, θ'_F for bulk F = Fe or Ni including the conversion at the F/$NbSe_2$ interface, for different choices of q. The values of the spin Hall angles in the bottom row are stable within the single-digit decimal precision over the entire interval of q. The uncertainty of the values is roughly 10%.

	θ_{NbSe_2} [%]	θ'_{Fe} [%]	θ'_{Ni} [%]	λ_N [nm]
$q = 1.0$	−1.5	0.5	–	0.8
$q = 0.9$	−1.1	0.3	1.5	0.9
$0.1 < q < 0.8$	−0.2	−0.5	1.2	5.5 – 6.1

non-monotonic trend of the Fe-based sample set, we choose $q = 0.9$. A more detailed description of the fitting results, including more values of λ_N and q, is given in Table S1 and Figure S6, Supporting Information. Consistent with our qualitative observations above, the inferred spin Hall angle θ_{NbSe_2} ranges from about − 1.1% (for λ_N = 0.9 nm) down to approximately −0.2% ($\lambda_N > 4$ nm). If we allow λ_N to be a free parameter, the fits yield solutions depending on q, as shown in **Table 1** and by the dark grey boundary curves in Figure 3 for $q = 0.5$ and 0.9. They support our qualitative model insights: The transport is either characterized by $\theta_{NbSe_2} \approx -1\%$ and $\lambda_N \approx 1$ nm, or a negligible θ_{NbSe_2} and a rather unusually large $\lambda_N \approx 6$ nm.[24,28,40,45,58]

2.8. Discussion

The inferred values of θ'_{Ni} and θ'_{Fe} are in reasonable agreement with literature magnitudes of around 1%.[21,40,62] While our analysis confirms the expected $\theta'_{Ni} > 0$,[24,44,45,58] the small value of θ'_{Fe} does not allow for a clear statement on the sign of θ'_{Fe}, considering that these quantities contain also the interfacial contribution of possibly similar magnitude but possibly different polarity.[40] The opposite signs of the inferred θ'_{Ni} and θ_{NbSe_2} provide an explanation of why the amplitudes of the emission signals from Ni and Fe-based sample sets are reversed (Figure 3): The dominant S2C and, thus, I_c in the two sample sets have opposite polarities.

To further discuss the inferred spin Hall angles of $NbSe_2$, we performed ab initio calculations of the spin Hall conductivity σ_{SH} for an out-of-plane-propagating spin current with in-plane spin polarization (see details in the Experimental Section and calculations in Figure S7, Supporting information). We obtain $\sigma_{SH} = -20$ S/cm at the Fermi level and a local minimum of −31 S/cm at 0.13 eV below. Considering the mean measured conductivity of $\sigma_{NbSe_2} = 2.2\times10^3$ S/cm in Fe|$NbSe_2$ and Ni|$NbSe_2$ (see Figure S4, Supporting Information), the expected spin Hall angle $\theta_{NbSe_2} = \sigma_{SH}/\sigma_{NbSe_2}$ lies in the interval −(0.9–1.4)%. This value, including its sign, is excellently consistent with the value $\theta_{NbSe_2} \approx -1\%$ extracted from our experiment (Figure 3) for scenario 1 with the shorter $\lambda_N \approx 1$ nm. Owing to the metallic nature of the 2H phase of $NbSe_2$ and the high density of states around the Fermi level,[63–65] we do not expect any strong dependence of the S2C in $NbSe_2$ on the optical pump wavelength, in contrast to a highly photon-energy-dependent spin injection in semiconducting TMDCs.[22]

Even though our experiment and theory agree well, we emphasize that our quantitative analysis has to be taken with caution because of a potentially large uncertainty of model parameters and non-trivial model assumptions. Formulated more conservatively, we conclude that the spin Hall angle of $NbSe_2$ is negative and has a magnitude larger than 1%. The corresponding THz spin-current relaxation length λ_N is of the order of a few nanometers.

We note that the extracted values might also be affected by a possible contribution of magnetic-dipole radiation to the THz signal, which arises from ultrafast demagnetization.[35] However, the d_N-dependence and opposite polarity of the emitted signal in Fe and Ni-based sample sets (Figure 2) rule out a dominant role of this effect in the total signal. This notion is corroborated by the fact that well reversed THz signals are found when the samples are rotated by 180° about the magnetization (see Figure S3, Supporting Information). The amplitude of magnetic-dipole emission is even under this operation, whereas the emission amplitude arising from spin transport and S2C is odd since j_s reverses its polarity.[35] Our test experiment indicates that a maximum contribution of magnetic-dipole radiation of 20% to the THz signal is possible. By rescaling and fitting the respective amplitude data in Figure 3, the quantitative analysis yields the same values as summarized in Table 1 within the given error bars of 10%. As the test experiment does not require any reference samples, there is no uncertainty related to growth reproducibility. Therefore, we consider the possible impact of the magnetic-dipole radiation negligible for our experiment.

3. Conclusion

We performed THz emission spectroscopy on ultra-high-vacuum-grown epitaxial stacks composed of layers of the TMDC $NbSe_2$ with varying thicknesses and of a ferromagnetic metal. Using qualitative analysis of the emitted THz pulses after optical excitation, we infer that the in-plane spin-polarized current is injected from the ferromagnet into the TMDC on ultrafast time scales. By comparison of the different thickness dependence of the emission from Fe-vs Ni-based sample sets to a spin-current model, we conclude that there is either a S2C in the bulk of TMDC with THz spin current relaxation length of ≈1 nm, or no significant conversion happens but the THz spin current relaxation length in the TMDC has a less realistic value above 4 nm. A quantitative analysis, based on fitting the model to the measured data, confirms the qualitative notion and yields the spin Hall angle of $NbSe_2$ in the range −(1.1–0.2)% with corresponding spin current relaxation lengths of 1–6 nm. Our findings show that ultrafast spin-current injection into the TMDC $NbSe_2$ is possible and that broadband THz emission spectroscopy[27,36,38,41,45,66] is an excellent and versatile tool for such investigations that complements the established THz methods.[56,67,68]

4. Experimental Section

Sample Preparation: Atomically thin films of $NbSe_2$ (2, 3, 4, 6 ML) were deposited by the hybrid-PLD.[42,43] Double-polished *c*-cut sapphire substrates were used as a substrate. The growth temperature was 500 °C as monitored by an infrared pyrometer working around a wavelength of 10 µm. Fluxes of pure Nb (99.9%) and Se (99.999%) were applied for a

duration calculated from a growth rate of ≈10 min ML^{-1} established by measuring the thickness of a reference sample using X-ray reflectivity (XRR) at a synchrotron light source.[42] The films were annealed at 400 °C under Se flux for 1 h after growth. Subsequently, the sample was capped with Se (15 nm) at room temperature. The capped samples were transferred through ambient air into another chamber, where the Se capping layer was removed by heating (150 °C). Subsequently, magnetic films of Fe or Ni (3 nm) were deposited by electron-beam evaporation. Finally, the heterostructure films were capped in situ with Al (2 nm) which readily oxidized in air to serve as an AlO_x protection layer. The 2H phase of $NbSe_2$ films was confirmed by scanning transmission electron microscopy. It contains variants of 2H stacking, including 2Ha (180° rotation between the layers) and 2Hb (0° rotation), consistent with the definitions in Ref. [69]

Spin-Current Model: To model spin-current propagation in an F|N stack with a semitransparent F/N interface, we consider the configuration in Figure 1. The F|N layers are stacked along the coordinate z with the origin set at the interface: the TMDC (layer N, thickness d_N) is located at $z > 0$, the ferromagnet (layer F, thickness d_F) at $z < 0$. The interface is characterized by the spin-current transmission coefficient $0 < t_s < 1$ and reflectivity coefficient $r_s = -1 + t_s < 0$. The reflection at the right sample boundary (N side) is considered using the coefficient $r_s' < 0$. As the spin-current relaxation length fulfills $\lambda_F \ll d_F$ in the F layer, we do not account for any effect of the left boundary.

By considering first a very thick N layer ($\lambda_N \ll d_N$), the spin current j_{s0} created at $z = 0$ after the optical excitation follows an exponential profile $j_s(z) = j_{s0}e^{z/\lambda_F}$ in F ($z < 0$) and $j_s(z) = j_{s0}e^{-z/\lambda_N}$ in N ($z > 0$).

If we consider realistic thicknesses of N and allow for back-reflections off the N boundary at $z = d_N$, the echos form an infinite sequence, yielding in N, that is, for $z \in [0, d_N]$,

$$\frac{j_s(z)}{j_{s0}} = e^{-z/\lambda_N} + r_s' e^{-2d_N/\lambda_N} e^{z/\lambda_N} + r_s' r_s e^{-2d_N/\lambda_N} e^{-z/\lambda_N} + \left(r_s' r_s\right)^2 e^{-4d_N/\lambda_N} e^{z/\lambda_N} + \cdots = \frac{1}{1-q_N}\left[\exp\left(\frac{-z}{\lambda_N}\right) + r_s' \exp\left(\frac{-2d_N + z}{\lambda_N}\right)\right] \quad (5)$$

where $q_N = r_s' r_s e^{-2d_N/\lambda_N}$.

Similarly, in F, that is, for $z \in [-d_F, 0]$, we have

$$\frac{j_s(z)}{j_{s0}} = \left[1 + \frac{t_s r_s'}{1-q_N}\exp\left(\frac{-2d_N}{\lambda_N}\right)\right]\exp\frac{z}{\lambda_N} \quad (6)$$

This solution still fulfils continuity of $j_s(z)$ at $z = 0$. The layer-integrated spin currents in N, F, and at the interface (I) are obtained by

$$J_N(d_N) = \int_0^{d_N} dz\ j_s(z) = j_{s0}\frac{\lambda_N}{1-q_N}\left[1 - \exp\left(\frac{-d_N}{\lambda_N}\right)\right]\left[1 + r_s' \exp\left(\frac{-d_N}{\lambda_N}\right)\right] \quad (7a)$$

$$J_F(d_N) = \int_{-\infty}^{0} dz\ j_F(z) = j_{s0}\lambda_F\left[1 + \frac{t_s r_s'}{1-q_N}\exp\left(\frac{-2d_N}{\lambda_N}\right)\right] \quad (7b)$$

$$J_I(d_N) = \int_{-d_I}^{0} dz\ j_F(0) = J_F(d_N) d_I/\lambda_F \quad (7c)$$

In the last integral, we assume that the interface is described by a very thin interlayer of effective thickness d_I over which the spin current j^I is approximately constant and equals $j_I = j_s(0)$.

By taking $r_s' = -1$, we obtain Equation (3). A possible spin memory loss a is included in the model by considering that t_s and r_s do not add up to unity: $t_s - r_s = 1 + a$ where $-1 < a < 0$, and by taking $-1 < r_s' < 0$.

Determination of Spin Hall Angles: The proportion $\theta_{NbSe_2} : \theta_{Fe}' : \theta_{Ni}'$ of the spin Hall angles, but not their absolute value, can be determined by fitting Equation (4) with the corresponding θ_F' and calculated J_F, J^N on two sets of data in Figure 3. To estimate the value of the spin Hall angles, the data were complemented by simultaneous measurements of two reference samples Fe|Pt and Ni|Pt. Similarly, to data in Figure 3, the RMS of their signals $S(t)$ were normalized to the corresponding pump light absorptance $A = 59.8\%$ and 61.5% and impedance $Z = 40.5\ \Omega$ and 38.9 Ω, respectively, obtaining normalized rms $I_c^{Fe|Pt}$ and rms $I_c^{Ni|Pt}$.

In accordance to Equation (1), we can expect that the S2C in these reference samples will be dominated by conversion in Pt ($\theta_F \ll \theta_{Pt} \approx 10\%$) and, thus,[24]

$$\text{rms } I_c^{F|Pt} = e\theta_{Pt} J_{Pt} = e\theta_{Pt}\lambda_{Pt}\frac{1}{d_F + d_{Pt}}\tanh\frac{d_{Pt}}{2\lambda_{Pt}} \quad (8)$$

where J_{Pt} is the integrated spin current in Pt, including a possible back-reflection using $r_s = r_s' = -1$, and other quantities with the same meaning as in the main text. For both sets with F = Fe and Ni and N = $NbSe_2$, we obtain the following two equations with two unknowns θ_F' and θ^N:

$$\frac{\text{rms } I_c^{F|N}}{\text{rms } I_c^{F|Pt}} = C_F = \frac{\theta_F' J_F + \theta_N J_N}{\theta_{Pt} J_{Pt}} \quad (9a)$$

$$D_F = \frac{\theta_N}{\theta_F'} \quad (9b)$$

Here, C_F are experimental inputs, D_F are known from fitting, spin currents J_F, J_N, and J_{Pt} are calculated using Equations (7) and (8), $\theta_{Pt} \approx 10\%$ and $\lambda_{Pt} = 1$ nm are taken as reference values from the literature.[21,40,45] Since we use only the ratio of simultaneously measured rms I_c in Equation (9a), all F-specific factors affecting the emission process are canceled out. Solving Equation (9) for both F yields

$$\theta_N = C_F\theta_{Pt}\frac{J_{Pt}}{J_F/D_F + J_N} \quad (10a)$$

$$\theta_F' = C_F\theta_{Pt}\frac{J_{Pt}}{J_F + J_N/D_F} \quad (10b)$$

Ab Initio Calculations: Density functional calculations are performed for the bulk $NbSe_2$ with an in-plane lattice constant of 3.44 Å. The distance between the van der Waals layers is 2.89 Å. The generalized gradient approximation of Perdew–Burke–Ernzerhof[70] is used for the exchange-correlation potential as implemented in the FLEUR code.[71] The maximally localized Wannier functions are constructed using the WANNIER90 code in conjunction with the FLEUR package,[72,73] based on which an effective Hamiltonian in a tight-binding scheme is constructed for the calculation of the DC spin Hall conductivity σ_{ij}^I according to

$$\sigma_{ij}^I = e\hbar\int\frac{d^3k}{(2\pi)^3}\sum_{n=1}^{N_{occ}}\Omega_{n,ijl}^S(k) \quad (11)$$

$$\Omega_{n,ijl}^S(k) = -2\text{Im}\sum_{m\neq n}\frac{\langle\psi_{mk}|J_i^{l,s}|\psi_{nk}\rangle\langle\psi_{nk}|v_j|\psi_{mk}\rangle}{(E_{nk} - E_{mk})^2} \quad (12)$$

Here, $\Omega_n^S(k)$ is the spin Berry curvature of all occupied states, v_j is the j-th Cartesian component of the velocity operator, $|\psi_{nk}\rangle$ is the Bloch function of band n at wave vector k with energy E_{nk}, and $J_i^{l,s} = (\hbar/2)\{\sigma_i, v_l\}$ describes a spin current flowing into direction i with a spin polarization along the l axis.

Supporting Information

Supporting Information is available from the Wiley Online Library or from the author.

Acknowledgements

The authors acknowledge funding by the German Research Foundation through the collaborative research center SFB TRR 227 "Ultrafast spin dynamics" (Project ID 328545488, projects A05, B02, and B10), the European Union H2020 program through the projects CoG TERAMAG (Grant No. 681917) and ASPIN (Grant No. 766566), the DFG priority program INTEREST (project ITISA), the Czech Science Foundation through Project GA CR (Grant No. 21–28876J), and the Grant Agency of the Charles University (Grant No. SVV–2022–260590). Y.M. acknowledges funding from Deutsche Forschungsgemeinschaft (DFG, German Research Foundation) — TRR 288 — 422213477 (Project B06). Y.M. acknowledges the Jülich Supercomputing Centre for providing computational resources under Project No. jiff40. A.B.-P. acknowledges support by the Generalitat Valenciana (CIDEGENT/2021/005). H.N. thanks I. Lakemeyer for her support in preparing the magnetic films.

Open access funding enabled and organized by Projekt DEAL.

Conflict of Interest

The authors declare no conflict of interest.

Data Availability Statement

The data that support the findings of this study are available from the corresponding author upon reasonable request.

Keywords

spin Hall angles, spin-to-charge-current conversion, terahertz emission spectroscopy, transition-metal dichalcogenides (TMDCs), ultrafast spin current injections

Received: July 28, 2022
Revised: August 30, 2022
Published online: October 20, 2022

[1] S. Manzeli, D. Ovchinnikov, D. Pasquier, O. V. Yazyev, A. Kis, *Nat. Rev. Mater.* **2017**, *2*, 17033.
[2] H. Zeng, J. Dai, W. Yao, D.i Xiao, X. Cui, *Nat. Nanotechnol.* **2012**, *7*, 490.
[3] L. Yang, W. Chen, K. M. Mccreary, B. T. Jonker, J. Lou, S. A. Crooker, *Nano Lett.* **2015**, *15*, 8250.
[4] L. Yang, N. A. Sinitsyn, W. Chen, J. Yuan, J. Zhang, J. Lou, S. A. Crooker, *Nat. Phys.* **2015**, *11*, 830.
[5] T. Yan, S. Yang, D. Li, X. Cui, *Phys. Rev. B* **2017**, *95*, 241406.
[6] S. Kar, Y. Su, R. R. Nair, A. K. Sood, *ACS Nano* **2015**, *9*, 12004.
[7] B. Fallahazad, H. C.P. Movva, K. Kim, S. Larentis, T. Taniguchi, K. Watanabe, S. K. Banerjee, E. Tutuc, *Phys. Rev. Lett.* **2016**, *116*, 086601.
[8] G. Aivazian, Z. Gong, A. M. Jones, R.-L. Chu, J. Yan, D. G. Mandrus, C. Zhang, D. Cobden, W. Yao, X. Xu, *Nat. Phys.* **2015**, *11*, 148.
[9] A. A. Mitioglu, P. Plochocka, Á. Granados Del Aguila, P. C. M. Christianen, G. Deligeorgis, S. Anghel, L. Kulyuk, D. K. Maude, *Nano Lett.* **2015**, *15*, 4387.
[10] R. Bertoni, C. W. Nicholson, L. Waldecker, H. Hübener, C. Monney, U. De Giovannini, M. Puppin, M. Hoesch, E. Springate, R. T. Chapman, C. Cacho, M. Wolf, A. Rubio, R. Ernstorfer, *Phys. Rev. Lett.* **2016**, *117*, 277201.
[11] M. M. Ugeda, A. J. Bradley, Y. Zhang, S. Onishi, Y. Chen, W. Ruan, C. Ojeda-Aristizabal, H. Ryu, M. T. Edmonds, H.-Z. Tsai, A. Riss, S.-K. Mo, D. Lee, A. Zettl, Z. Hussain, Z.-X. Shen, M. F. Crommie, *Nat. Phys.* **2015**, *12*, 92.
[12] J. Kim, C. Jin, B. Chen, H. Cai, T. Zhao, P. Lee, S. Kahn, K. Watanabe, T. Taniguchi, S. Tongay, M. F. Crommie, F. Wang, *Sci. Adv.* **2017**, *3*, 1700518.
[13] J. R. Schaibley, H. Yu, G. Clark, P. Rivera, J. S. Ross, K. L. Seyler, W. Yao, X. Xu, *Nat. Rev. Mater.* **2016**, *1*, 16055.
[14] A. Kormányos, V. Zólyomi, N. D. Drummond, G. Burkard, *Phys. Rev. X* **2014**, *4*, 011034.
[15] L. Bawden, S. P. Cooil, F. Mazzola, J. M. Riley, L. J. Collins-McIntyre, V. Sunko, K. W. Hunvik, M. Leandersson, C. M. Polley, T. Balasubramanian, T. K. Kim, M. Hoesch, J. W. Wells, G. Balakrishnan, M. S. Bahramy, P. D. King, *Nat. Commun.* **2016**, *7*, 11711.
[16] D.i Xiao, G.-B. Liu, W. Feng, X. Xu, W. Yao, *Phys. Rev. Lett.* **2012**, *108*, 196802.
[17] Q. Shao, G. Yu, Y.-W. Lan, Y. Shi, M.-Y. Li, C. Zheng, X. Zhu, L.-J. Li, P. K. Amiri, K. L. Wang, *Nano Lett.* **2016**, *16*, 7514.
[18] K. F. Mak, K. L. Mcgill, J. Park, P. L. Mceuen, *Science* **2014**, *344*, 1489.
[19] C. Cheng, M. Collet, J.-C. R. Sánchez, V. Ivanovskaya, B. Dlubak, P. Seneor, A. Fert, H. Kim, G. H. Han, Y. H. Lee, H. Yang, A. Anane, arXiv: 1510.03451v2 **2016**.
[20] W. Zhang, J. Sklenar, B.o Hsu, W. Jiang, M. B. Jungfleisch, J. Xiao, F. Y. Fradin, Y. Liu, J. E. Pearson, J. B. Ketterson, Z. Yang, A. Hoffmann, *APL Mater.* **2016**, *4*, 032302.
[21] J. Sinova, S. O. Valenzuela, J. Wunderlich, C. H. Back, T. Jungwirth, *Rev. Mod. Phys.* **2015**, *87*, 1213.
[22] L. Cheng, X. Wang, W. Yang, J. Chai, M. Yang, M. Chen, Y. Wu, X. Chen, D. Chi, K. E. J. Goh, J.-X. Zhu, H. Sun, S. Wang, J. C. W. Song, M. Battiato, H. Yang, E. E. M. Chia, *Nat. Phys.* **2019**, *15*, 347.
[23] T. Kampfrath, M. Battiato, P. Maldonado, G. Eilers, J. Notzold, S. Mahrlein, V. Zbarsky, F. Freimuth, Y. Mokrousov, S. Blugel, M. Wolf, I. Radu, P. M. Oppeneer, M. Münzenberg, *Nat. Nanotechnol.* **2013**, *8*, 256.
[24] T. Seifert, S. Jaiswal, U. Martens, J. Hannegan, L. Braun, P. Maldonado, F. Freimuth, A. Kronenberg, J. Henrizi, I. Radu, E. Beaurepaire, Y. Mokrousov, P. M. Oppeneer, M. Jourdan, G. Jakob, D. Turchinovich, L. M. Hayden, M. Wolf, M. Münzenberg, M. Kläui, T. Kampfrath, *Nat. Photonics* **2016**, *10*, 483.
[25] R. Schneider, M. Fix, J. Bensmann, S. Michaelis De Vasconcellos, M. Albrecht, R. Bratschitsch, *Appl. Phys. Lett.* **2019**, *115*, 152401.
[26] Y. Sasaki, K. Z. Suzuki, S. Mizukami, *Appl. Phys. Lett.* **2017**, *111*, 102401.
[27] T. J. Huisman, R. V. Mikhaylovskiy, J. D. Costa, F. Freimuth, E. Paz, J. Ventura, P. P. Freitas, S. Blugel, Y. Mokrousov, T. Rasing, A. V. Kimel, *Nat. Nanotechnol.* **2016**, *11*, 455.
[28] G. Li, R. V. Mikhaylovskiy, K. A. Grishunin, J. D. Costa, T.h Rasing, A. V. Kimel, *J. Phys. D: Appl. Phys.* **2018**, *51*, 134001.
[29] T. S. Seifert, S. Jaiswal, J. Barker, S. T. Weber, I. Razdolski, J. Cramer, O. Gueckstock, S. F. Maehrlein, L. Nadvornik, S. Watanabe, C. Ciccarelli, A. Melnikov, G. Jakob, M. Münzenberg, S. T. B. Goennenwein, G. Woltersdorf, B. Rethfeld, P. W. Brouwer, M. Wolf, M. Kläui, T. Kampfrath, *Nat. Commun.* **2018**, *9*, 2899.
[30] O. Gueckstock, R. L. Seeger, T. S. Seifert, S. Auffret, S. Gambarelli, J. N. Kirchhof, K. I. Bolotin, V. Baltz, T. Kampfrath, L. Nádvorník, *Appl. Phys. Lett.* **2022**, *120*, 062408.
[31] E. Rongione, O. Gueckstock, M. Mattern, O. Gomonay, H. Meer, C. Schmitt, R. Ramos, E. Saitoh, J. Sinova, H. Jaffrès, M. Mičica, J. Mangeney, S. T. B. Goennenwein, S. Geprägs, T. Kampfrath, M. Kläui, M. Bargheer, T. S. Seifert, S. Dhillon, R. Lebrun, arXiv: 2205.11965 **2022**.
[32] D. Yagodkin, L. Nádvorník, O. Gueckstock, C. Gahl, T. Kampfrath, K. I. Bolotin, *2D Mater.* **2021**, *8*, 025012.
[33] T. Seifert, S. Jaiswal, M. Sajadi, G. Jakob, S. Winnerl, M. Wolf, M. Kläui, T. Kampfrath, *Appl. Phys. Lett.* **2017**, *110*, 252402.

[34] O. Gueckstock, L. Nádvorník, T. S. Seifert, M. Borchert, G. Jakob, G. Schmidt, G. Woltersdorf, M. Kläui, M. Wolf, T. Kampfrath, *Optica* **2021**, *8*, 1013.
[35] R. Rouzegar, L. Brandt, L. Nadvornik, D. A. Reiss, A. L. Chekhov, O. Gueckstock, C. In, M. Wolf, T. S. Seifert, P. W. Brouwer, G. Woltersdorf, T. Kampfrath, arXiv: 2103.11710 **2021**.
[36] T. S. Seifert, L. Cheng, Z. Wei, T. Kampfrath, J. Qi, *Appl. Phys. Lett.* **2022**, *120*, 180401.
[37] L. Cheng, Z. Li, D. Zhao, E. E. M. Chia, *APL Mater.* **2021**, *9*, 070902.
[38] W. Wu, C. Yaw Ameyaw, M. F. Doty, M. B. Jungfleisch, *J. Appl. Phys.* **2021**, *130*, 091101.
[39] J. Cramer, T. Seifert, A. Kronenberg, F. Fuhrmann, G. Jakob, M. Jourdan, T. Kampfrath, M. Kläui, *Nano Lett.* **2018**, *18*, 1064.
[40] O. Gueckstock, L. Nádvorník, M. Gradhand, T. S. Seifert, G. Bierhance, R. Rouzegar, M. Wolf, M. Vafaee, J. Cramer, M. A. Syskaki, G. Woltersdorf, I. Mertig, G. Jakob, M. Kläui, T. Kampfrath, *Adv. Mater.* **2021**, *33*, 2006281.
[41] M. Meinert, B. Gliniors, O. Gueckstock, T. S. Seifert, L. Liensberger, M. Weiler, S. Wimmer, H. Ebert, T. Kampfrath, *Phys. Rev. Appl.* **2020**, *14*, 064011.
[42] A. Mohammed, H. Nakamura, P. Wochner, S. Ibrahimkutty, A. Schulz, K. Müller, U. Starke, B. Stuhlhofer, G. Cristiani, G. Logvenov, H. Takagi, G. Logvenov, *Appl. Phys. Lett.* **2017**, *111*, 073101.
[43] H. Nakamura, A. Mohammed, P. Rosenzweig, K. Matsuda, K. Nowakowski, K. Küster, P. Wochner, S. Ibrahimkutty, U. Wedig, H. Hussain, J. Rawle, C. Nicklin, B. Stuhlhofer, G. Cristiani, G. Logvenov, H. Takagi, U. Starke, *Phys. Rev. B* **2020**, *101*, 165103.
[44] H. Wang, C. Du, P. Chris Hammel, F. Yang, *Appl. Phys. Lett.* **2014**, *104*, 202405.
[45] T. S. Seifert, N. M. Tran, O. Gueckstock, S. M. Rouzegar, L. Nadvornik, S. Jaiswal, G. Jakob, V. V. Temnov, M. Münzenberg, M. Wolf, M. Kläui, T. Kampfrath, M. Wolf, *J. Phys. D: Appl. Phys.* **2018**, *51*, 364003.
[46] J. Hawecker, T. H. Dang, E. Rongione, J. Boust, S. Collin, J. M. George, H. J. Drouhin, Y. Laplace, R. Grasset, J. Dong, J. Mangeney, J. Tignon, H. Jaffrès, L. Perfetti, S. Dhillon, J. Dong, *Adv. Opt. Mater.* **2021**, *9*, 2100412.
[47] Y. Wu, M. Elyasi, X. Qiu, M. Chen, Y. Liu, L. Ke, H. Yang, *Adv. Mater.* **2017**, *29*, 1603031.
[48] J. Walowski, M. Münzenberg, *J. Appl. Phys.* **2016**, *120*, 140901.
[49] G. Torosyan, S. Keller, L. Scheuer, R. Beigang, E. Th. Papaioannou, *Sci. Rep.* **2018**, *8*, 1311.
[50] S. Zhang, Z. Jin, Z. Zhu, W. Zhu, Z. Zhang, G. Ma, J. Yao, *J. Phys. D: Appl. Phys.* **2018**, *51*, 034001.
[51] Y. Liu, H. Cheng, Y. Xu, P. Vallobra, S. Eimer, X. Zhang, X. Wu, T. Nie, W. Zhao, *Phys. Rev. B* **2021**, *104*, 064419.
[52] C. Bull, S. M. Hewett, R. Ji, C.-H. Lin, T. Thomson, D. M. Graham, P. W. Nutter, *APL Mater.* **2021**, *9*, 090701.
[53] M. Matthiesen, D. Afanasiev, J. R. Hortensius, T. C. Van Thiel, R. Medapalli, E. E. Fullerton, A. D. Caviglia, *Appl. Phys. Lett.* **2020**, *116*, 212405.
[54] A. Leitenstorfer, S. Hunsche, J. Shah, M. C. Nuss, W. H. Knox, *Appl. Phys. Lett.* **1999**, *74*, 1516.
[55] T. Kampfrath, J. Nötzold, M. Wolf, *Appl. Phys. Lett.* **2007**, *90*, 231113.
[56] L. Nádvorník, M. Borchert, L. Brandt, R. Schlitz, K. A. De Mare, K. Výborný, I. Mertig, G. Jakob, M. Kläui, S. T. B. Goennenwein, M. Wolf, G. Woltersdorf, T. Kampfrath, *Phys. Rev. X* **2021**, *11*, 021030.
[57] D. L. Mills, *Nonlinear Optics: Basic Concepts*, Springer, Berlin **1998**.
[58] D. Yang, J. Liang, C. Zhou, L. Sun, R. Zheng, S. Luo, Y. Wu, J. Qi, *Adv. Opt. Mater.* **2016**, *4*, 1944.
[59] A. F. Rigosi, H. Hill, S. Krylyuk, N. V. Nguyen, A. R. Hight Walker, A. V. Davydov, D. B. Newell, *J Res Natl Inst Stand Technol* **2019**, *124*, 124035.
[60] H. M. Hill, A. F. Rigosi, S. Krylyuk, J. Tian, N. V. Nguyen, A. V. Davydov, D. B. Newell, A. R. Hight Walker, *Phys. Rev. B* **2018**, *98*, 165109.
[61] A. Castellanos-Gomez, N. Agraït, G. Rubio-Bollinger, *Appl. Phys. Lett.* **2010**, *96*, 213116.
[62] Q.i Zhang, Z. Luo, H. Li, Y. Yang, X. Zhang, Y. Wu, *Phys. Rev. Appl.* **2019**, *12*, 054027.
[63] J. Á. Silva-Guillén, P. Ordejón, F. Guinea, E. Canadell, *2D Mater.* **2016**, *3*, 035028.
[64] Y. Nakata, K. Sugawara, R. Shimizu, Y. Okada, P. Han, T. Hitosugi, K. Ueno, T. Sato, T. Takahashi, *NPG Asia Mater.* **2016**, *8*, 321.
[65] B. Riccò, *Phys. Status Solidi* **1976**, *77*, 287.
[66] F. N. Kholid, D. Hamara, M. Terschanski, F. Mertens, D. Bossini, M. Cinchetti, L. McKenzie-Sell, J. Patchett, D. Petit, R. Cowburn, J. Robinson, J. Barker, C. Ciccarelli, *Appl. Phys. Lett.* **2021**, *119*, 032401.
[67] J. J. F. Heitz, L. Nádvorník, V. Balos, Y. Behovits, A. L. Chekhov, T. S. Seifert, K. Olejník, Z. Kašpar, K. Geishendorf, V. Novák, R. P. Campion, M. Wolf, T. Jungwirth, T. Kampfrath, *Phys. Rev. Appl.* **2021**, *16*, 064047.
[68] N. A. Goncharuk, L. Nádvorník, C. Faugeras, M. Orlita, L. Smrčka, *Phys. Rev. B* **2012**, *86*, 155409.
[69] H. Katzke, P. Tolédano, W. Depmeier, *Phys. Rev. B* **2004**, *69*, 134111.
[70] J. P. Perdew, K. Burke, M. Ernzerhof, *Phys. Rev. Lett.* **1996**, *77*, 3865.
[71] Stefan Blügel, FLEUR-project, www.flapw.de (accessed: October 2022).
[72] A. A. Mostofi, J. R. Yates, Y.-S.u Lee, I. Souza, D. Vanderbilt, N. Marzari, *Comput. Phys. Commun.* **2008**, *178*, 685.
[73] F. Freimuth, Y. Mokrousov, D. Wortmann, S. Heinze, S. Blügel, *Phys. Rev. B* **2008**, *78*, 089902.